POLITECNICO DI TORINO
Repository ISTITUZIONALE

LONG-DISTANCE, DRAG-FREE, LOW-THRUST, LEO FORMATION CONTROL FOR EARTH GRAVITY MONITORING

Terms of use:

Publisher copyright

(Article begins on next page)

19 April 2024

LONG-DISTANCE, DRAG-FREE, LOW-THRUST, LEO FORMATION CONTROL FOR EARTH GRAVITY MONITORING

Enrico Canuto[1], Andrés Molano-Jimenez[1], Carlos Perez-Montenegro[1], Luca Massotti[2]

[1]Politecnico di Torino, Dipartimento di Automatica e Informatica

Corso Duca degli Abruzzi 24, 10129 Torino, Italy, (e-mail: enrico.canuto@polito.it)

[2]ESA Earth Observation Future Missions Division,

ESTEC EOP-SF, Noordwijk NL-220 AG, The Netherlands(e-mail: luca.massotti@esa.int)

ABSTRACT

The formation control of a long-distance, drag-free, low-thrust, low-Earth orbit satellite is outlined, in view of future Earth-gravity monitoring missions employing long baseline interferometry (> 10 km) and lasting at least six years. To this purpose, a formation consisting of two drag-free satellites, orbiting at a fixed distance in a sun-synchronous orbit, has been proposed. Formation fluctuations are bounded by a 500x50x50 m wide (along-track, cross-track and radial) box. Although at first not seemingly demanding, the formation control induces non-gravitational accelerations, that are obliged to respect tight drag-free requirements, and are constrained by millinewton thrust bounds so as to curtail electric thruster throttability. In addition, formation fluctuations due to tide forces should not be impaired as their measurement is the mission goal. Requirements are formulated as a set of four time and frequency–domain inequalities, which are suitably parameterized by control gains. By exploiting the properties and asymptotic approximations of close-loop Hill's equation, explicit design inequalities are obtained leading to a first-trial control design. Simulated runs through fine spacecraft and low-Earth-orbit simulation, which is dominated by a highly variable thermosphere drag, show that the first-trial design meets the tight control requirements, and demonstrates mission feasibility.

KEYWORDS : Satellite formation, drag-free, control, low-thrust, low-Earth-orbit

1   INTRODUCTION

The paper addresses the formation control of a pair of satellites in a low-Earth orbit at a long distance, up to 100 km during a 6-year mission [1]. The mission adheres to the European Space Agency (ESA) requirements of the Next Generation Gravimetry Missions that aim to measure the temporal variations of the Earth gravity field over a long time span like GRACE (Gravity Recovery And Climate Experiment, seven year mission, launched in 2002, [2]), but with a higher time resolution than the GRACE monthly time base. A time sampling of one week or shorter has been identified as mandatory to reduce the level of aliasing that affects high frequency geophysical phenomena as encountered in the GRACE data. Spatial resolution on the Earth surface needs to be as good as GOCE (Gravity field and steady state Ocean Circulation Explorer, two-year mission, launched in 2009, [3],[4]), that means better than 100 km.

The formation distance is fixed by the baseline of an interferometric gradiometer created by the pair of satellites as in the GRACE mission (220 km distance), which in contrast with GRACE, are forced to free fall by cancelling their non gravitational forces (drag-free control). Thus the differential acceleration becomes highly sensible to the local gravity tensor, less non gravitational residuals that should be kept below a pre-specified target. The differential acceleration and the gravity tensor parameters are achieved by processing the formation fluctuations measured by an inter-satellite laser interferometer, and the satellite drag-free accelerations measured by GOCE-class accelerometers, the latter having a noise floor better than 3×10^{-12} m/$\left(s^2 \sqrt{\text{Hz}} \right)$ in the frequency range from 1 to 100 mHz. Laser pointing accuracy is guaranteed by fine satellite alignment (attitude control) and by the formation displacements remaining within a $500 \times 50 \times 50$ m box (formation control) for a 10-km distance. The latter should be considered a tight constraint as it is tailored to J2 differential fluctuations. Satellite-to-satellite laser tracking is mandatory to meet a distance variation measurement with a noise floor lower than 10 nm/$\sqrt{\text{Hz}}$. In comparison, the K-band range system of the GRACE formation had a noise floor of about 10 μm/$\sqrt{\text{Hz}}$.

All-propulsion actuation has been selected by discarding magnetic bearing reaction wheels as attitude actuators because of vibration/noise limits on the laser metrology. Reduction of propellant and thruster mass in a 6-year mission can only rely on scalable and throttable electric propulsion. An already-flown, scalable, though low-throttable thruster technology, such as micro-RIT propulsion (radio-frequency thrusters [5]) is under study and test in view of its fitting to mission requirements. A layout of nine thrusters (one redundant) has been designed (Figure 1) from the heritage of the early GOCE design [4], [6], [7], later abandoned because of immature technology. One redundant mini-thruster (< 20 mN) is dedicated to along-track drag-free and formation control. Eight micro-thrusters (< 1.2 mN) in a balanced configuration are dedicated to lateral formation, drag-free and attitude control. The symmetric configuration allows the thrust to be biased so as to overcome minimum thrust limitations, though at the cost of propellant consumption.
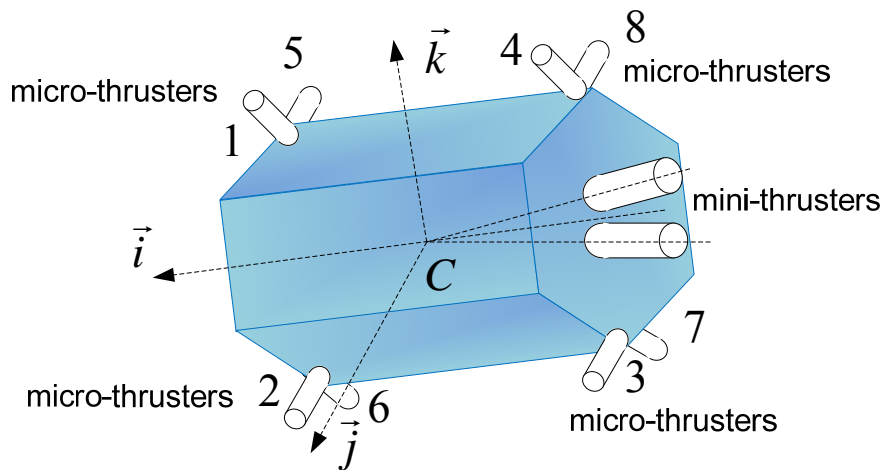

Figure 1 Single satellite shape and thruster layout.

The main limitation comes from a poor throttability range (<10) compared to the wide and unprecedented ratio (up to 40) requested by a long-term drag-free mission at low-Earth orbit. A 6-year drag-free mission must bear the extreme drag conditions of the thermosphere that are due to variable solar and geomagnetic activities (Figure 2).
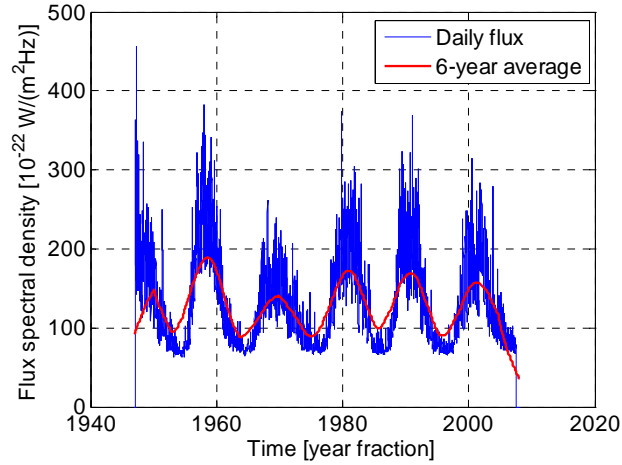
Figure 2   Historical solar activity index.

Throttability may be attenuated by correlating orbit altitude with the expected average solar activity; nevertheless high solar activity is accompanied by wide fluctuations, leading to the throttability target of 40 (Figure 2). The overall control design, combining drag-free, attitude and formation control, must be guaranteed to stay below thrust upper bound under normal conditions, and to smoothly degrade under thruster saturation.

The paper outlines a formation control design capable of respecting thruster bounds together with formation and drag-free requirements for a total of three norm inequalities (Section 3.1). Formation control causes each satellite to accelerate in a non-gravitational way, and this must be kept within drag-free limits. Drag-free control is fed by non-gravitational accelerations that are obtained by processing the on-board accelerometer data. Formation control is fed by differential GPS range and rate, which are affected by the differential acceleration that includes the differential gravity (tide force) to be measured by the mission. It is therefore mandatory that the formation command be sufficiently decoupled from gravity components, adding a further norm inequality (the fourth one) to control design. To the author's knowledge, no formation control of this kind has so far been studied (see [8], [9] and [10]).

Formation dynamics endowed with stochastic disturbance dynamics (see [7] and [11]) is outlined in Section 2, and proved in the Appendix. Similar to [12] and [13], it accounts for eccentricity and J2 which render state equations periodic. Due to low eccentricity (<0.5%) the

control design is approached in Section 3 with a linear, time-invariant approximation, where periodic terms play the role of input perturbations. The linear control law includes reference command, tracking errors and disturbance rejection [11], but the focus here is on the design of tracking error gains (feedback command), which are capable of respecting design inequalities. The reference generator and state predictor, the latter being in charge of predicting controllable and disturbance state variables, are not considered here. It is shown that closed-loop eigenvalues can be decoupled, without impairing the tuning/optimizing capability of the feedback gains with respect to the design inequalities. A first-trial and explicit design is shown, based on the series expansion of the periodic input perturbations and on the asymptotic expansion of the closed-loop transfer functions. The esign performance is demonstrated by the simulated results in Section 4. The latter have been obtained with a fine simulator of the formation and of the low-Earth-orbit environment, thereby making a long-term mission critical because of the thermosphere drag.

2   FORMATION DYNAMICS

2.1   Reference orbit and frame

The following notations will be employed: arrowed letters such as $\vec{r}$ denote vectors, bold letters such as $\mathbf{r}$ denote Cartesian coordinates in some frame of reference. The position and velocity of the Centre-of-Mass (CoM) of the spacecrafts are denoted with $\vec{r}_k$ and $\vec{v}_k$, $k = 0,1$, as in Figure 3. The formation CoM position $\vec{r}$ and velocity $\vec{v}$, and the corresponding differential vectors $\varDelta\vec{r}$ and $\varDelta\vec{v}$, are defined assuming that both spacecrafts have equal mass, namely

$$\begin{aligned}\vec{r} = (\vec{r}_0 + \vec{r}_1)/2, \ \vec{v} = (\vec{v}_0 + \vec{v}_1)/2 \\ \varDelta\vec{r} = \vec{r}_0 - \vec{r}_1, \ \varDelta\vec{v} = \vec{v}_0 - \vec{v}_1\end{aligned} \qquad (1)$$

The differential coordinates

$$\varDelta\mathbf{r} = \mathbf{r}_0 - \mathbf{r}_1 = \begin{bmatrix} \varDelta x & \varDelta z & \varDelta y \end{bmatrix}^T, \ \varDelta\mathbf{v} = \mathbf{v}_0 - \mathbf{v}_1 = \begin{bmatrix} \varDelta v_x & \varDelta v_z & \varDelta v_y \end{bmatrix}^T \qquad (2)$$

of $\Delta\vec{r}$ and $\Delta\vec{v}$, along-track, radial and cross-track, are expressed (3) in the Local Orbital Frame (LORF)

$$\left\{C, \vec{i}_O = v/|\vec{v}|, \vec{j}_O = \vec{r} \times \vec{v}/|\vec{r} \times \vec{v}|, \vec{k}_O = \vec{i}_O \times \vec{j}_O\right\}, \tag{4}$$

which is attached to the drag-free orbit of C. The natural order of radial and cross-track entries is reversed in (2). The orbit of C is the combination of a reference near-circular orbit (point $\underline{C}$ of position $\underline{\vec{r}}$ in Figure 3) and a perturbation $\delta\vec{r}$. The CoM perturbation $\delta\vec{r}$ and the differential position $\Delta\vec{r}$ can be expressed through the vector $\delta\vec{r}_k = \overrightarrow{\underline{C}C_k}$ as in (1):

$$\begin{aligned} \delta\vec{r} &= \left(\delta\vec{r}_0 + \delta\vec{r}_1\right)/2 \\ \Delta\vec{r} &= \delta\vec{r}_0 - \delta\vec{r}_1 \end{aligned} . \tag{5}$$
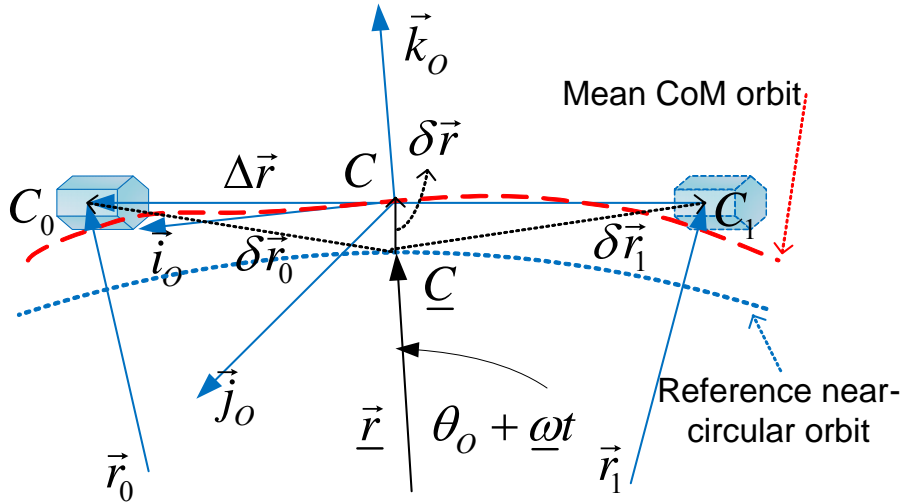

Figure 3   Formation geometry and local orbital frame.

The orbit of C and the associated frame are materialized by averaging on-board GPS measurements and retrieving the LORF quaternion through a suitable state predictor as in [14]. The main component of the perturbation $\delta\vec{r}$ is a drift caused by the drag-free residual bias, as a result of the on-board accelerometer offset. The drift rate $\left|\delta\dot{\vec{r}}\right| \cong 500$ m/day is a common-mode error not affecting formation dynamics. The latter is instead affected by the differential drift to be actively rejected as shown below.

2.2 Formation dynamics and perturbations

The formation dynamics, derived and proved in the Appendix for a near-polar orbit $i \cong \pi/2$, lead to the following linear, time-invariant equation, written with the radial and cross-track coordinates in a reverse order as in (2):

$$
\begin{bmatrix} \Delta\dot{\mathbf{r}} \\ \Delta\dot{\mathbf{v}} \\ \dot{\mathbf{x}}_d \end{bmatrix}(t) = \begin{bmatrix} A_r & I & 0 \\ -\Omega^2 & A_v & I \\ 0 & 0 & 0 \end{bmatrix} \begin{bmatrix} \Delta\mathbf{r} \\ \Delta\mathbf{v} \\ \mathbf{x}_d \end{bmatrix}(t) + \begin{bmatrix} 0 \\ I \\ 0 \end{bmatrix} \left(\Delta\mathbf{u}(t) + \mathbf{g}(\theta) \right) + \begin{bmatrix} 0 \\ \mathbf{w}_a \\ \mathbf{w}_d \end{bmatrix}(t). \tag{6}
$$

Sub-matrices and vectors in (6)can be found to be

$$
A_r = \begin{bmatrix} 0 & -2\underline{\omega} & 0 \\ 0 & 0 & 0 \\ 0 & 0 & 0 \end{bmatrix}, \; A_v = \begin{bmatrix} 0 & 0 & 0 \\ 2\underline{\omega} & 0 & 0 \\ 0 & 0 & 0 \end{bmatrix}, \; \Omega^2 = \begin{bmatrix} 0 & 0 & 0 \\ 0 & \underline{\omega}_z^2 & 0 \\ 0 & 0 & \underline{\omega}_y^2 \end{bmatrix}. \tag{7}
$$

Measurements are provided by on-board differential GPS as outlined in Section 3.7. The forcing functions are the formation command $\Delta\mathbf{u}$, the periodic function $\mathbf{g}(\theta)$ defined in the Appendix, and the wide-band noise vectors $\mathbf{w}_a$ and $\mathbf{w}_d$, generating the stochastic process

$$
\mathbf{d}(t) = \mathbf{x}_d(t) + \mathbf{w}_a(t). \tag{8}
$$

The vector $\mathbf{d}$, sum of the random drift $\mathbf{x}_d$ and of the noise $\mathbf{w}_a$, accounts for drag-free residuals and thruster noise according to [7] and [11]. The command $\Delta\mathbf{u}$ is implemented by dispatching opposite components to each spacecraft, i.e.

$$
\Delta\mathbf{u} = \mathbf{u}_0 - \mathbf{u}_1, \; \mathbf{u}_0 = \Delta\mathbf{u}/2, \; \mathbf{u}_1 = -\mathbf{u}_0 \; . \tag{9}
$$

In this way the peak command is halved in favor of constraint (14). The differential drag-free residual $\Delta\mathbf{a}$ includes formation command $\Delta\mathbf{u}$ and is defined by

$$
\Delta\mathbf{a}(t) = \mathbf{d}(t) + \Delta\mathbf{u}(t) = \Delta\mathbf{a}_d(t) + \Delta\mathbf{a}_h(\theta). \tag{10}
$$

The last sum in (10) splits residuals into random components $\Delta\mathbf{a}_d$ and periodic components $\Delta\mathbf{a}_h(\theta)$. The orbit frequencies $\underline{\omega} \cong 1.2$ mrad/s, $\underline{\omega}_z$ and $\underline{\omega}_y$ are defined in the Appendix, and show a slight discrepancy due to J2 and eccentricity. Discrepancies lead to a long-term beat visible in Figure 7. The following lemma is straightforward.

Lemma 1. The eigenvalues of (6) are the square root of the diagonal entries of $-\Omega^2$, i.e.

$$\lambda_{x0,x1} = 0, \; \lambda_{z0,z1} = \pm j\underline{\omega}_z, \; \lambda_{y0,y1} = \pm j\underline{\omega}_y. \tag{11}$$

Lemma 1 shows (6) is unstable. A bounded free response might be obtained with suitable initial conditions, which are of no interest here, since $\Delta\mathbf{r}$ must be kept bounded under the disturbance in (6).

Formation state predictor and control are designed and implemented around a discrete-time version of (6), where the wide-band noise vectors $\mathbf{w}_a$ and $\mathbf{w}_d$ become discrete-time white noise with bounded variance, and the time unit T is designed such that $\omega T \ll 1$.

2.3 Actuator layout and bounds

Drag-free, formation and attitude control have been designed to be all–propulsion.. Figure 1 shows the baseline shape of a single satellite and the layout of the thruster assembly, which consists of a pair of mini-thrusters (one redundant, 0.45 to 18 mN) and of eight micro-thrusters (0.05 to 2 mN). Bounds on the disturbance signals $g_j(\theta) + d_j$, $j = x, z, y$, and on the command entries Δu_j in (6) are listed in Table 1.

No.	Type (symbol)	Along-track [mN]	Radial [mN]	Cross-track [mN]
0	Generic disturbance d_j			
0.1	Accelerometer bias	0.06	6 (reduced to 0.06)	0.06
0.2	Accelerometer drift	negligible	0.004	negligible
1	Periodic disturbance $> J_2$, $g_j(\theta)$			
1.1	Gravity, $> J_2$	0.5	0.5	0.1
1.2	Gravity, J_2	33	37	negligible
1.3	Eccentricity e	50	negligible	negligible
2	Command Δu_j			

Table 1. Bounds to perturbations and command

2.1	Force bound $F_{k,\max}$	1.5	1.2	1.2 (micro-thrusters)
		(mini-thruster)	(micro-thruster)	
2.2	Acceleration $\left[\mu \text{m/s}^2 \right]$	3	2.4	2.4

The values in rows 0.1 and 0.2 derive from the typical noise of the GOCE-class accelerometers, which differ from axis to axis. Table 1 shows that the radial bias is incompatible with command limits. The force bound in Table 1, row 2.1, is an absolute value restricted to formation axes, which has been computed by allocating 20% of the peak thrust to formation. The last row converts force into acceleration through the satellite mass $m = 500 \text{ kg}$. Thrust allocation in Table 1, rows 2.1 and 2.2, has been traded-off with drag-free and attitude control authority. The disturbance overshoot in Table 1, rows 0.1, 1.2 and 1.3, may be avoided in two ways. Radial accelerometer bias, row 0.1, should be reduced either by re-design or by bias estimation before the drag-free control is activated. Gravity and eccentricity perturbations, rows 1.2 and 1.3, are periodic with ω and of higher order. Formation control should avoid their rejection.

3   Control objectives and design

3.1   Control objectives

Formation objectives are derived assuming drag-free control is operating on each satellite. Unlike drag-free control where the control is fed with the measurements of non gravitational accelerations provided by on-board accelerometers, the formation control is fed by differential position and rate, depending on the overall differential acceleration: gravity anomalies, eccentricity contribution and drag-free residuals. This implies that formation commands might cross-couple with gravitational anomalies, a condition to be avoided especially inside the mission measurement bandwidth (MBW) defined by

$$f_0 = 1 \text{ mHz} \le f \le f_1 = 10 \text{ mHz} , \tag{12}$$

and corresponding to the minimum of the dashed bowl-shaped profile in Figure 4.
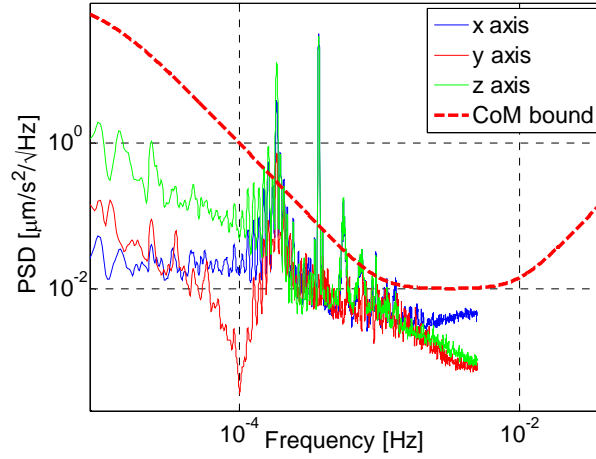
Figure 4 Spectral density of the target and simulated non gravitational accelerations.

The control objectives are formulated as a set of inequalities to be respected by the control gains.

The formation bound is a time-domain constraint. The tracking error $\delta\mathbf{r} = \Delta\mathbf{r} - \Delta\underline{\mathbf{r}}$ is defined with respect to a reference displacement, equal, at the end of the formation acquisition phase, to $\Delta\underline{\mathbf{r}}^T = \begin{bmatrix} d & 0 & 0 \end{bmatrix}$. The tracking error box is defined by

$$
\left| W_r \delta\mathbf{r} \right|_\infty \leq \delta r_{\max} = 50 \text{ m}, \\
W_r = \text{diag}\left\{ w_{rx} << 1, 1, 1 \right\}
$$
(13)

The thrust bound is a time-domain constraint defined by

$$
\left| W_u \Delta\mathbf{u} \right|_\infty \leq \Delta u_{\max} = 2.4 \ \mu\text{m/s}^2 \\
W_u = \text{diag}\left\{ w_{ux} < 1, 1, 1 \right\}
$$
(14)

The drag-free bound is a frequency-domain inequality involving the spectral density matrix of the random differential drag-free residuals $\Delta\mathbf{a}_d$ in (10), as follows

$$
\sigma_{\max}\left(\mathbf{S}_a^2(f) \right) \leq \left| \mathbf{V}_a(jf) \right| \Delta a_{\max}, \\
\Delta a_{\max} \leq 0.01 \ \mu\text{m/s}^2 / \sqrt{\text{Hz}}
$$
(15)

where $\sigma_{\max}$ denotes the root of the largest eigenvalue, $\left| \mathbf{V}_a(f) \right| \geq 1$ is bowl-shaped as in Figure 4 and $\Delta a_{\max}$ is the bound inside the MBW (12).

10

The periodic component $\Delta\mathbf{a}_h$ of the drag-free residuals must decouple from the periodic function $\mathbf{g}(\theta)$ especially in the MBW (12), i.e.

$$\max_f \sigma_{\max}\left(\mathbf{V}\left(jf\right)\right) \leq \sigma_{h,\max} = 10^{-3}, f \geq f_0,\tag{16}$$

where $\mathbf{V}$ is the closed-loop transfer function from the unrejected disturbance $\mathbf{g} + \mathbf{w}_a$ to $\Delta\mathbf{u}$ in (18), and $\sigma_{\max}$ is the max singular value.

3.2   The control law

Similar to [7] and [11], the control law combines tracking and disturbance rejection in

$$\Delta\mathbf{u}(t) = \Delta\underline{\mathbf{u}}(t) - \left(K_r\delta\mathbf{r} + K_v\Delta\mathbf{v} + \mathbf{x}_d\right),\tag{17}$$

where $\Delta\underline{\mathbf{u}}(t) = 0$ as soon as formation acquisition has been achieved. As a control strategy, the periodic term $\mathbf{g}(\theta)$ does not appear in (17), since it must not be rejected for two different reasons:

1)   eccentricity and J2 components overshoot the thruster bound as shown in Table 1,

2)   periodic components higher than J2 are the mission objective, and must not be cancelled from the relative formation position as entailed by inequality (16).

Control design aims to find gain matrices K_r and K_v capable of satisfying constraints (13) to (16).

The law (17) must be kept as ideal, as it is affected by the measurement errors through the state predictor [14] (see Section 3.7). On the other hand, the ideal law (17) is incapable of fully rejecting the stochastic disturbance $\mathbf{d}$ in (8) because of causality, leaving the unpredictable noise $\mathbf{w}_a$ to force the tracking error. Notice that $\mathbf{w}_a$ includes all unpredictable sources as, for instance, prediction errors. The closed-loop transfer functions to be used below easily follow on from (6) and (17) as

$$\begin{aligned}
\Delta\mathbf{a}(s) &= \left(I - \mathbf{V}(s)\right)\mathbf{w}_a(s) - \mathbf{V}(s)\mathbf{g}(s) \\
\Delta\mathbf{r}(s) &= -\mathbf{S}(s)\mathbf{M}(s)\left(\mathbf{w}_a(s) + \mathbf{g}(s)\right) \\
\Delta\mathbf{u}(s) &= -\mathbf{V}(s)\left(\mathbf{w}_a(s) + \mathbf{g}(s)\right) - s^{-1}\mathbf{w}_d(s)
\end{aligned}\tag{18}$$

where

$$\mathbf{V}(s) = \mathbf{C}(s)\mathbf{S}(s)\mathbf{M}(s)$$
$$\mathbf{S}(s) = \left(I + \mathbf{C}(s)\mathbf{M}(s)\right)^{-1},$$

(19)

and

$$\mathbf{C}(s) = K_r + K_v s$$

$$\mathbf{M}(s) = \mathbf{D}_m^{-1}(s)\begin{bmatrix} \left(s^2 + \underline{\omega}_z^2 - 4\underline{\omega}^2\right)/s^2 & -2\underline{\omega}/s & 0 \\ 2\underline{\omega}/s & 1 & 0 \\ 0 & 0 & 1 \end{bmatrix}.$$

(20)

$$\mathbf{D}_m(s) = \mathrm{diag}\left\{s^2 + \underline{\omega}_z^2, s^2 + \underline{\omega}_z^2, s^2 + \underline{\omega}_y^2\right\}$$

3.3   Design steps

It is shown how to reduce the four inequalities (13) to (16) to a pair and how to make their expressions dependent on the feedback gains in (17). Time-domain inequalities (13) and (14) are tackled by expanding the tracking errors and command components into the following harmonic series of the orbit mean angular frequency $\underline{\omega}$ defined in the Appendix

$$\delta\mathbf{r}(t) = \delta\mathbf{r}_d(t) + W_r^{-1}\delta r_{\max}\sum_{k=1}^{\infty}\mathbf{a}_h\sin\left(k\underline{\omega}t + \varphi_k\right)$$

$$\left\|\sum_{k=1}^{\infty}|\mathbf{a}_h|\right\|_{\infty} \leq 1, \ \mathbf{a}_k^T = \begin{bmatrix} a_{kx} & a_{kz} & a_{ky} \end{bmatrix}$$

(21)

where $\delta\mathbf{r}_d$ is a zero-mean random component to be kept as negligible with respect to the periodic component, since $\mathbf{g}(\theta)$ is not rejected. As the forcing frequency $\underline{\omega}$ is very close to $\underline{\omega}_y$ and $\underline{\omega}_z$, forcing (17) with a series like (21) generates a bounded beat motion as mentioned in Section 2.2 and proved by a high-fidelity simulation (Figure 7). The series coefficients follow from the closed-loop transfer functions of (6) and (17), and from expanding $\mathbf{g}(\theta)$ as in (21): as such they include the control gains in (17).

An approximate, worst-case solution is adopted. The tracking error coefficients in (21) are kept equal to their peak values, which makes them independent of the control gains. Inserting (21) into (17) provides a series expansion of $\Delta\mathbf{u}(t)$ whose coefficients depend on the control gains. Using such a series in (14) results in the first design inequality .

The second design inequality is obtained by showing that only inequality (16) affects control gains, whereas inequality (15) establishes sensor and actuator noise as in Section 3.7. In fact

$\mathbf{V}$ is a low-pass filter whose high-frequency asymptote is shaped by K_r and K_v; moreover the bandwidth of $\mathbf{V}$ must be sufficiently smaller than the lower limit f_0 of the MBW (12) so as to guarantee (16). This is formulated by the limit

$$\lim_{f > f_0} \left(I - \mathbf{V}(jf) \right) \to I, \tag{22}$$

and by the fact that $\mathbf{S}_a^2(f)$ in (15) is just the spectral density of the wide-band noise $\mathbf{w}_a$. The latter, summing up high-frequency accelerometer noise, thruster noise and sensor noise, allows them to be allocated. Furthermore, using (19), and observing that $\mathbf{S}(jf)$ satisfies a limit such as (22), the high-frequency asymptote holds

$$\lim_{f > f_0} \mathbf{V}(jf) = \lim_{f \to \infty} \mathbf{C}(jf) \mathbf{M}(jf) = \frac{K_v}{j 2 \pi f} \begin{bmatrix} 1 & -\omega(j\pi f)^{-1} & 0 \\ \omega(j\pi f)^{-1} & 1 & 0 \\ 0 & 0 & 1 \end{bmatrix}. \tag{23}$$

The next step is to find a suitable parameterization of the control gains, making the solution of (14) and (16) explicit and feasible.

3.4 Decoupled closed-loop eigenvalue design

Control gain parameterization passes through a decoupled eigenvalue design and the closed-loop Hill's equation properties. To this end, the controllable part of (6) and the control law (17) can be rearranged as follows

$$\begin{bmatrix} \dot{\mathbf{x}}_x \\ \dot{\mathbf{x}}_z \\ \dot{\mathbf{x}}_y \end{bmatrix}(t) = \begin{bmatrix} A_{xx} & A_{xz} & 0 \\ A_{zx} & A_{zz} & 0 \\ 0 & 0 & A_{yy} \end{bmatrix} \begin{bmatrix} \mathbf{x}_x \\ \mathbf{x}_z \\ \mathbf{x}_y \end{bmatrix}(t) + \begin{bmatrix} B & 0 & 0 \\ 0 & B & 0 \\ 0 & 0 & B \end{bmatrix} \begin{bmatrix} \Delta u_x + x_{dx} + w_{ax} + g_x \\ \Delta u_z + x_{dz} + w_{az} + g_z \\ \Delta u_y + x_{dy} + w_{ay} + g_y \end{bmatrix}(t)$$
$$\begin{bmatrix} \Delta u_x \\ \Delta u_z \\ \Delta u_y \end{bmatrix}(t) = - \begin{bmatrix} K_{xx} & K_{xz} & K_{xy} \\ K_{zx} & K_{zz} & K_{zy} \\ K_{yx} & K_{yz} & K_{yy} \end{bmatrix} \begin{bmatrix} \mathbf{x}_x \\ \mathbf{x}_z \\ \mathbf{x}_y \end{bmatrix}(t) - \begin{bmatrix} x_{dx} \\ x_{dz} \\ x_{dy} \end{bmatrix}(t) \tag{24}$$

with the following matrices and vectors

$$A_{xx} = \begin{bmatrix} 1 & 1 \\ 0 & 1 \end{bmatrix}, \ A_{xz} = \begin{bmatrix} -2\underline{\omega} & 0 \\ 0 & 0 \end{bmatrix}, \ B = \begin{bmatrix} 0 \\ 1 \end{bmatrix}$$

$$A_{zx} = \begin{bmatrix} 0 & 0 \\ 0 & 2\underline{\omega} \end{bmatrix}, \ A_{zz} = \begin{bmatrix} 1 & 1 \\ -\omega_z^2 & 0 \end{bmatrix}, \ A_{yy} = \begin{bmatrix} 1 & 0 \\ -\omega_y^2 & 0 \end{bmatrix}. \tag{25}$$

$$\mathbf{x}_x = \begin{bmatrix} \delta x \\ \Delta v_a \end{bmatrix}, \ \mathbf{x}_z = \begin{bmatrix} \delta z \\ \Delta v_z \end{bmatrix}, \ \mathbf{x}_y = \begin{bmatrix} \delta y \\ \Delta v_y \end{bmatrix}$$

The first step is to fix closed-loop eigenvalues that guarantee the bounded-input-bounded-output stability of (24) and (17). Following Lemma 1 and the decoupling inequality (16), the following closed-loop eigenvalues are selected

$$\lambda_{x0} = -p_{x0} < 0, \ \lambda_{x0} = -p_{x1} < 0$$
$$\lambda_{z0,z1} = \left(-\zeta_z \pm j\sqrt{1-\zeta_z^2}\right)\omega_z, \quad , \tag{26}$$
$$\lambda_{y0,y1} = \left(-\zeta_y \pm j\sqrt{1-\zeta_y^2}\right)\omega_y$$

where the first pair refers to the longitudinal motion to be bounded in position and rate, the second and third ones to radial and cross-track displacements that must be weakly damped so as not to degrade gravitational components.

Feedback gains that guarantee (26) follow from the results below. The first one is straightforward.

Result 1. Since the cross-track dynamics in (24) are fully decoupled from longitudinal and radial dynamics, the feedback matrix in (24) reduces to

$$K = \begin{bmatrix} K_{xx} & K_{xz} & 0 \\ K_{zx} & K_{zz} & 0 \\ 0 & 0 & K_{yy} \end{bmatrix}. \tag{27}$$

Cross-track gains derive from a well-known result, which is hereafter stated and proved.

Result 2. Assuming $\left|g_y + w_{ay}\right|_\infty$ is bounded, a feedback matrix $K_{yy} = \begin{bmatrix} k_{ry} & k_{vy} \end{bmatrix}$ which stabilizes $A_{yy} - BK_{yy}$ and makes $\left|\Delta u_y\right|$ bounded in agreement with (14), is a damping feedback, i.e.

$$k_{ry} = 0, \ k_{vy} = 2\zeta_y \underline{\omega}_y, \tag{28}$$

where $\zeta_y > 0$ must be selected to be compatible with (16).

Proof. The cross-track command in (24), assuming zero open-loop command, namely $\Delta\underline{u}_y = 0$, and fixing the gains of K_{yy} to $k_{vy} = 2\zeta_y\underline{\omega}_y$ and $k_{ry} = \underline{\omega}_y^2$, becomes

$$\Delta u_y(t) = -2\zeta_y\omega_y\Delta v_y - \Delta\omega_y\left(\omega_y + \omega_y\right)\delta y - x_{dy}, \tag{29}$$

where $\Delta\omega_y = \omega_y - \underline{\omega}_y$. Solving the forced response in (24) under (29) leads to the inequality

$$\left|\Delta u_y(t)\right|_\infty \leq 2\zeta_y\omega_y\left|h_{\Delta v}(t) + h_{\Delta y}(t)\Delta\omega_y / \zeta_y\right|_1\left|g_y + w_{ay}\right|_\infty, \tag{30}$$

where $h_{\delta y}(t)$ and $h_{\Delta v}(t)$ are position and rate impulse responses. By exploiting the exponential decay of the impulse responses, (30) converts into

$$\left|\Delta u_y(t)\right|_\infty \leq 2\frac{\sqrt{1 - 2\Delta\omega_y / \omega_y + \left(\Delta\omega_y / \left(\zeta_y\omega_y\right)\right)^2}}{\sqrt{1 - \zeta_y^2}}\left|g_y + w_{ay}\right|_\infty, \tag{31}$$

and proves that $\left|\Delta u_y\right|$ is minimized by setting $\left|\Delta\omega_y\right| = 0$ and lowering $\zeta_y > 0$.

In order to apply Result 2 to the radial feedback, which amounts to assigning

$$k_{rz} = 0, \; k_{vz} = 2\zeta_z\underline{\omega}_z \tag{32}$$

in $K_{zz} = \begin{bmatrix} k_{rz} & k_{vz} \end{bmatrix}$, the longitudinal and radial closed-loop dynamics in (24) must possess a decoupling property. Lemma 2 and Result 3 below provide the closed-loop matrix

$$\left[\begin{array}{c|c} A_{xx} - BK_{xx} & A_{xz} - BK_{xz} \\ \hline A_{zx} - BK_{zx} & A_{zz} - BK_{zz} \end{array}\right] \tag{33}$$

with the necessary property. Next Lemma follows from the characteristic polynomial of (33).

Lemma 2. A necessary and sufficient condition for the eigenvalues of (33) are equal to the eigenvalues of the diagonal matrices in (33), is that

$$\left(A_{zx} - BK_{zx}\right)\left(\lambda I - A_{xx} + BK_{xx}\right)^{-1}\left(A_{xz} - BK_{xz}\right) = 0. \tag{34}$$

Straightforward algebra in (34) leads to the following pair of first-degree polynomials in λ

$$\begin{array}{c} \lambda\left(2\underline{\omega}k_{rzx} + k\left(\underline{\omega}\right)k_{rxz}\right) + 2\underline{\omega}\left(k_{rzx}k_{vx} - k\left(\underline{\omega}\right)k_{rx}\right) + k_{rxz}k_{rzx} = 0 \\ \left(k\left(\underline{\omega}\right)\lambda + k_{rzx}\right)k_{vxz} = 0, \; k\left(\underline{\omega}\right) = k_{vzx} - 2\underline{\omega} \end{array}, \tag{35}$$

that must be solved in the four gains of $K_{xz} = \begin{bmatrix} k_{rxz} & k_{vxz} \end{bmatrix}$ and $K_{zx} = \begin{bmatrix} k_{rzx} & k_{vzx} \end{bmatrix}$. A pair of solutions exist, but only the second one allows $\left|W_u\Delta\mathbf{u}\right|_\infty$ to be bounded.

1) The first solution, called rate-decoupling, follows by zeroing the non zero entry in A_{zx} in (24), and holds

$$k_{rzx} = k_{rxz} = k_{vxz} = 0, \ k_{vzx} = 2\underline{\omega}. \tag{36}$$

2) The second solution, called position-decoupling, yields the equalities

$$k_{rxz} = k_{rzx} = k_r = -\underline{\omega}k_{vx}\left(1 \pm \sqrt{1 - 4k_{rx}/k_{vx}^2}\right), \ k_{vzx} = k_{vxz} = 0, \tag{37}$$

through some manipulation.

By adopting (37), the following result can be stated.

Result 3. Feedback gains (28), (32) and (37) lead to a control law which can be fully tuned through four parameters: the damping coefficients ζ_y, ζ_z, and the eigenvalues $\{\lambda_{xj} = -p_{xj}\}$, $j = 0,1$, the latter of which set the gains in $K_{xx} = [k_{rx} \quad k_{vx}]$.

Proof. The proof follows by writing

$$k_{rx} = p_{x0}p_{x1}, \ k_{vx} = p_{x0} + p_{x1}, \tag{38}$$

and by observing that the non-zero gain in (37) is minimized by

$$k_r = -2p_x\underline{\omega}, \ p_x = \min\{p_{x0}, p_{x1}\}. \tag{39}$$

The formation command $\Delta\mathbf{u}$, which is now fully tunable, can be written as

$$\begin{aligned}
\Delta u_x &= -p_{x0}p_{x1}\delta x - (p_{x0} + p_{x1})\Delta v_x + 2\underline{\omega}p_x\delta z - x_{dx} \\
\Delta u_z &= -2\zeta_z\underline{\omega}_z\Delta v_z + 2\underline{\omega}p_x\delta x - x_{dz} \\
\Delta u_y &= -2\zeta_y\underline{\omega}_y\Delta v_y - x_{dy}
\end{aligned}, \tag{40}$$

where the components of $\mathbf{x}_d$ are estimated so as to respect the thrust bound (14).

In the following, for simplicity's sake, the design parameters are reduced to the pair

$$\zeta = \zeta_y = \zeta_z, \ p_x = p_{x0} = p_{x1}, \tag{41}$$

and the orbit frequencies are simplified to be equal as follows

$$\underline{\omega} = \underline{\omega}_z = \underline{\omega}_y. \tag{42}$$

3.5 Gain tuning

By assuming (41), the control law (40) is employed to solve inequalities (14) and (16) for the final parameters in (41). Let us start from the command inequality (14) which, by employing (40) and (21), can be rewritten as

$$
\begin{aligned}
\left|\Delta u_x\right| &\le p_x w_{rx}^{-1} \delta r_{\max} \sum_{k=1}^{\infty} \left(\left(p_x + 2\underline{\omega}k \right) \left|a_{kx}\right| + p_x 2\underline{\omega} \left|a_{kz}\right| w_{rx} \right) + x_{d,\max} \le w_{ux}^{-1} \Delta u_{\max} \\
\left|\Delta u_z\right| &\le 2\underline{\omega} \delta r_{\max} \sum_{k=1}^{\infty} \left(k\underline{\omega}\zeta \left|a_{kz}\right| + p_x \left|a_{kx}\right| w_{rx}^{-1} \right) + x_{d,\max} \le \Delta u_{\max} \\
\left|\Delta u_y\right| &\le 2\underline{\omega}^2 \zeta \delta r_{\max} \sum_{k=1}^{\infty} k \left|a_{ky}\right| + x_{d,\max} \le \Delta u_{\max}
\end{aligned}
\qquad (43)
$$

where $x_{d,\max}$ is the uniform bound of the entries of $\mathbf{x}_d$, that mainly depend on the accelerometer bias in Table 1.

A first-trial solution is achieved by assuming that the longitudinal pole is much smaller than the orbit frequency, i.e. $p_x << 2\underline{\omega}$, which condition simplifies the first inequality in (43) to

$$
p_x w_{rx}^{-1} \delta r_{\max} \sum_{k=1}^{\infty} 2\underline{\omega}k \left|a_{kx}\right| \le w_{ux} \Delta u_{\max} - a_{d,\max} .
\qquad (44)
$$

Furthermore, by allocating the same bound to both terms of $\left|\Delta u_z\right|$, by assuming that the first and second harmonic dominate the series in (43), and that the higher harmonics roll off with -40 dB/decade (Kaula's rule [15]), the solution splits into the design inequalities

$$
\begin{aligned}
\zeta &\le \left(\Delta u_{\max} - a_{d,\max} \right) \left(2\underline{\omega}^2 \delta r_{\max} \gamma \right)^{-1} \cong 5 \times 10^{-3} \\
p_x &\le \left(\Delta u_{\max} - a_{d,\max} \right) w_{rx} \left(4\underline{\omega} \delta r_{\max} \right)^{-1} \cong 10^{-6} \text{ rad/s} << 2\underline{\omega}
\end{aligned}
\qquad (45)
$$

where Kaula's rule has allowed replacing the sum in (44) with

$$
\sum_{k=1}^{\infty} k \left|a_{kj}\right| \le \gamma < 2, \ j = x, y, z .
\qquad (46)
$$

The numerical values in (45) may be iterated versus the actual position bounds, and especially versus the longitudinal bound, thus relaxing the worst-case assumption which lead to (43). For instance, as Figure 7 shows, the along-track component δx can be bounded below $\delta r_{\max}$ such as δz in (13). Thus one may set $w_x \cong 1$ in (13) and (45) and select p_x in (41) as a faster pole.

Let su now rewrite inequality (16) as

$$\sigma_{max} \left(\frac{-j}{\pi f_{min}} \begin{bmatrix} p_x & j\alpha p_x & 0 \\ -j\alpha\underline{\omega}\zeta & \zeta\underline{\omega} & 0 \\ 0 & 0 & \zeta\underline{\omega} \end{bmatrix} \right) \leq \sigma_{h,max} , \qquad (47)$$

$$\alpha = \left(\pi f_{min} \right)^{-1} \underline{\omega} < 1$$

having observed that the maximum in (16) occurs at $f = f_0$, that is on the left border of the MBW in (12), and having employed (23), (28), (32) (38), (41) and (42). Straightforward computation shows the largest singular value in (47) is bounded by

$$\left(\pi f_{min} \right)^{-1} \sqrt{\left(p_x^2 + \zeta^2 \underline{\omega}^2 \right) \left(1 + \alpha^2 \right)} \leq \sigma_{h,max} , \qquad (48)$$

which becomes a further design inequality. If the values in (45) and (16) satisfy (48), as it is the case, the first-trial design is complete. Notice however that increasing w_x and therefore p_x, as suggested above, may lead (48) not to be respected.

3.6 Gain scheduling

It has been previously remarked that the inequality (45), imposed by the command bound (14), might be relaxed without affecting (14), which allows to select a faster longitudinal pole p_x, and a higher radial and cross-track damping coefficient ζ . Such a design is desirable to speed up initial phases, such as formation acquisition and accelerometer bias tracking, being they useless for science. As such, mission inequalities (15), (16) and (48) do not apply during such phases. A two-phase gain scheduling strategy has been implemented as shown in the simulated runs. The switching time has been tuned on the faster poles of the initial phase. .

3.7 Sensors and measurement errors

The differential position and velocity coordinates are estimated from on-board GPS receivers. Requirements on GPS measurement errors are obtained by allocating a fraction $\gamma_u < 1$ of the residual acceleration bound in (15) to the formation command (40). The design inequalities (45) and the expected accelerometer bias in Table 1 suggest splitting the command components in (40) into dominant terms, and minor terms, the latter being denoted with δu_j, $j = x, y, z$. In this way, using simplifications (41) and (42), (40) becomes

$$
\begin{aligned}
\Delta u_x &= -2p_x\left(\Delta v_x - \underline{\omega}\delta z\right) + \delta u_x \\
\Delta u_z &= -2\zeta\underline{\omega}\Delta v_z + \delta u_z \\
\Delta u_y &= -2\zeta\underline{\omega}\Delta v_y + \delta u_z
\end{aligned}
\qquad , \qquad (49)
$$

Furthermore, by replacing Δv_j, δz, Δu_j and δu_j in (49) with the contribution of the measurements errors $\Delta\tilde{v}_j$, $\delta\tilde{z}$, $\Delta\tilde{u}_j$ and $\delta\tilde{u}_j$, equation (49) becomes an error equation. Now, by denoting the spectral density matrix of the command error $\Delta\tilde{\mathbf{u}}$ with $\mathbf{S}_{\Delta u}$, a design inequality similar to (15) is obtained

$$
\sigma_{\max}\left(\mathbf{S}_{\Delta\tilde{u}}^2\left(f\right)\right) \le \gamma_u\left|\mathbf{V}_a\left(jf\right)\right|\Delta a_{\max}, \qquad (50)
$$

where $\gamma_u < 1$ accounts for the allocated fraction of $\Delta a_{\max}$, and that half of the formation command is allocated to each spacecraft as in (9).

As a further step, the error components in (49) are expressed in terms of the differential GPS range and rate errors δr_k and δv_k, which results in

$$
\begin{aligned}
\delta\tilde{z} &= \delta r_z \\
\Delta\tilde{v}_x &= \delta v_x + \underline{\omega}\delta r_z \\
\Delta\tilde{v}_y &= \delta v_y \\
\Delta\tilde{v}_z &= \delta v_x - \underline{\omega}\delta r_x
\end{aligned}
\qquad . \qquad (51)
$$

The error spectral densities of a single GPS receiver are denoted with $S_{\delta r}^2$ (range) and $S_{\delta v}^2$ (rate), and are assumed to be equal for all components and receivers. By restricting to the diagonal entries of $\mathbf{S}_{\Delta\tilde{u}}^2$ in (50), a scalar inequality is found from (49) and (51), namely

$$
\sqrt{S_{\delta v}^2\left(f\right) + \underline{\omega}^2 S_{\delta r}^2\left(f\right)} \le \frac{1}{\sqrt{2}}\frac{\gamma_u\left|\mathbf{V}_a\left(jf\right)\right|\Delta a_{\max}}{2\max\left(p_x,\zeta\underline{\omega}\right)}. \qquad (52)
$$

Range and rate errors can be assigned separate bounds through a uniform apportioning of (52). The resulting spectral bounds are compared to GOCE-type receiver errors (obtained from on-ground tests) in Figure 5 and Figure 6. GOCE-type receivers should be improved to satisfy (52), especially for what concerns rate errors.
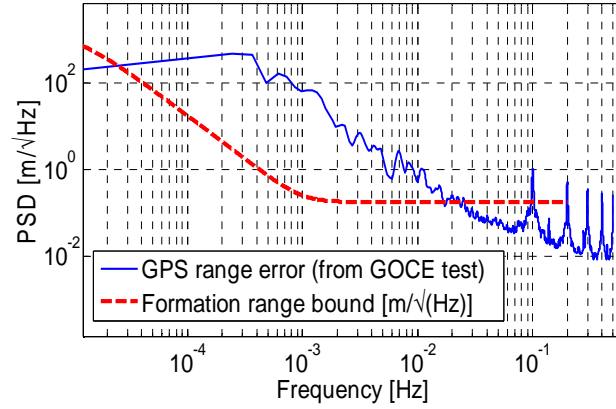
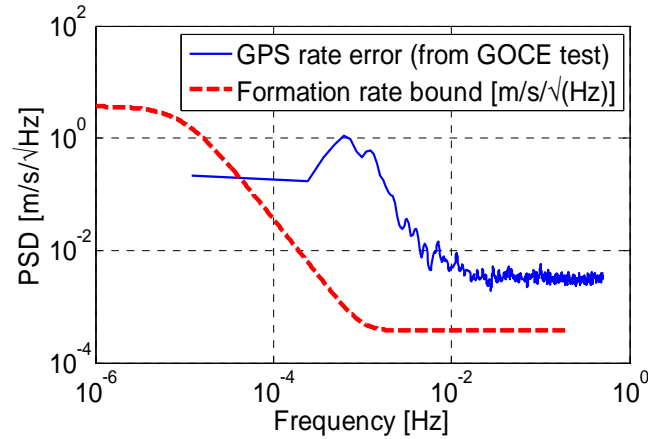Figure 5   Spectral bound of the GPS range error compared to GOCE-type error.

Figure 6   Spectral bound of the GPS rate error compared to GOCE-type error.

4   Simulated results

4.1   Simulated conditions

Simulated results have been obtained from an in-house fine simulator, and have been confirmed by the mission end-to-end simulator of Thales Alenia Space Italia, Torino, Italy. A sun-synchronous orbit has been simulated. The initial orbital elements are: inclination $i = 1.69 \, \text{rad}$, eccentricity $e_0 = 0.002$, geodetic altitude $h_0 = 325 \, \text{km}$, right ascension of the ascending node $\Omega_0 = 1.98 \, \text{rad}$, zero argument of perigee and zero true anomaly. To experience the worst-case low-Earth-orbit environment, an extreme solar activity index,

$F_{10.7} = 380 \times 10^{-22}$ W/m^2/Hz, has been assumed (see Figure 2), partly mitigated by an average geomagnetic index $A_p = 20$ nT.

The formation has been assumed to be already reached. Simulation lasts more than 5 Ms (about 2 months) so as to experience the formation beat motion generated by eccentricity and J2 as expected from (72). The accelerometer noise spectral density is bowl-shaped and can be found in [6]. Below 1 mHz, a 2nd order (bounded) drift builds up, which must be counteracted by formation control. Drift range is much lower than the bias as Table 1 shows. The whole ensemble of drag-free, formation and attitude control has been implemented, including reference generators, state predictors and control laws as in [14].

4.2 Simulated performance

The relative position residuals during a 2-month mission are shown in Figure 7The formation is assumed to start within the bounds (13) and close to a minimum (500 ks) of the beat motion. The latter naturally increases (and then decreases) inside the formation bounds: formation control must not reduce it, not to reach command saturation and degrade gravitational components. The long-term oscillation in Figure 7 modulates the amplitude of the orbit oscillations whose period is $2\pi / \underline{\omega} \cong 5400$ s.

Figure 8 shows the enlargement of Figure 7 at the simulation onset. The initial peak allows the accelerometer bias to be tracked. Closed-loop time constants are very long, close to one day, and are imposed by the low thrust limits in Table 1 as explained in Section 3. Gain scheduling has been implemented, and the wide-band initial phase, featuring a faster pole p_x than (45), ends at 600 ks, what is better appreciated in Figure 9.
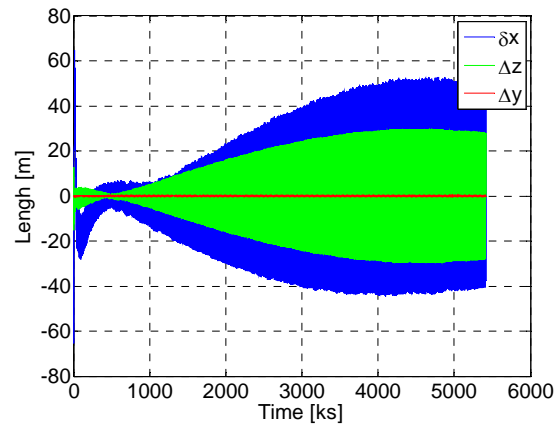
Figure 7   Residual relative position during 2-month mission.
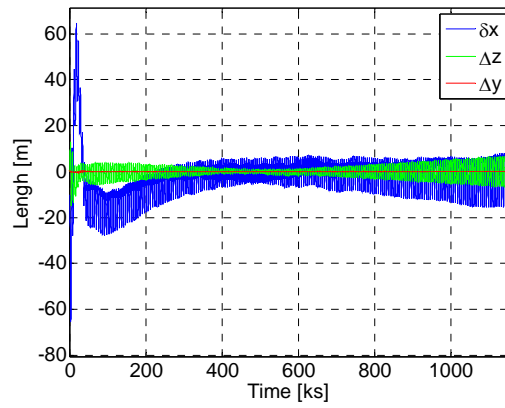

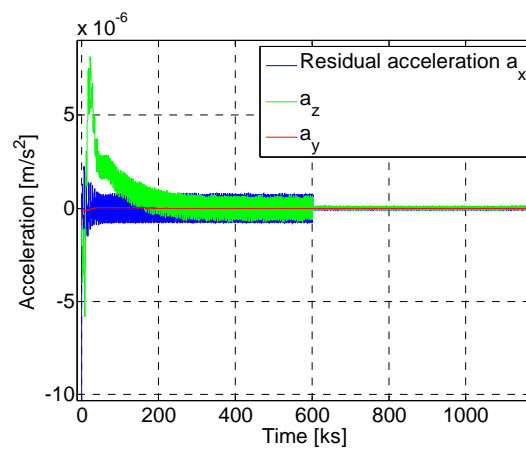Figure 8   Enlargement of Figure 7 at the onset.

Figure 9   Residual acceleration from wide- to narrow-band control.

Figure 9 shows the time profile of the residual non-gravitational acceleration which is requested to remain within the drag-free bound in (15). During the bias tracking, until 600 ks, the bound is not respected. Figure 4 shows the component spectral density of the residual non gravitational acceleration after 600 ks, when a narrow-band control, featuring the pole p_x in (45), is applied so as to converge to within the bound (15).. Overshoots in Figure 4 below the MBW frequency limit of 1 mHz, are due to non-zero radial and cross-track damping, spilling orbit harmonics (mainly first and second) into formation command, but respecting (16).

4.3   Thrust profiles, propellant consumption and electric power

Figure 10 shows the thrust profile of the micro-thrusters in Figure 1. Thrust reaches the admissible peak value just at the onset, that corresponds to the along-track peak in Figure 7. Control is robust against short-time saturation, but the latter should be avoided by constraining the mission to begin during low solar activity. One may notice that the average thrust in Figure 10 is lower than a 50% of the maximum allowable thrust. Allocating the higher 50% of the thrust range just to the accelerometer bias tracking and to high solar activity is such to increase propellant consumption as discussed below, since, during normal conditions, thrusters are forced to work around a lower specific impulse.
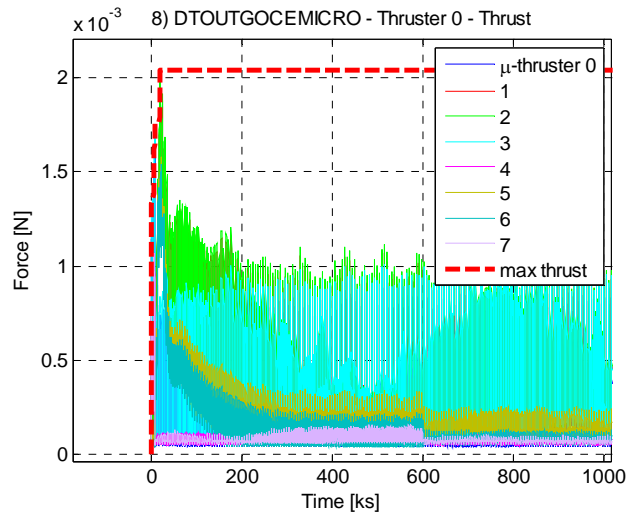

Figure 10 Thrust profile of the formation and attitude control.

Minimal propellant consumption was not mentioned as a formation control objective in Section 3.1. A key objective of the overall control system (drag-free, attitude and formation) was to guarantee the thruster assembly with a 6-year propellant consumption below 50 kg. Simulation runs under scaled micro-RIT performance (derived from experimental data) reported a total consumption of about 70 kg, 40% more than the target. The progressive 6-year propellant consumption of a single mini-thruster plus the eight micro-thrusters of Figure 1 is plotted in Figure 11.
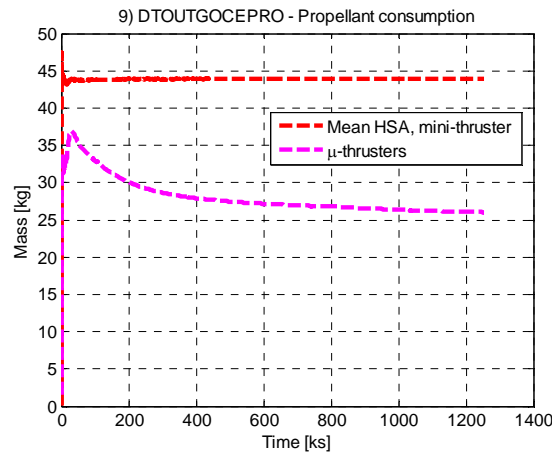

Figure 11 Progressive 6-year propellant consumption of mini and micro-thrusters.

The main reason of the propellant excess can be referred to a lower specific impulse of the scaled micro-RIT technology with respect to the scaled profile of the GOCE-type thrusters (Kaufman ion-thruster technology [16]) in the lower half of the thrust range, where thrusters are confined to work the main part of the mission as shown in Figure 10. The profiles in Figure 12, as they were scaled from experimental data, must be considered as study requirements. As a matter of fact, the target of 50 kg was estimated assuming GOCE-type thrusters, that subsequently were ruled out because not scalable and showing poor throttability at the study epoch. Propellant consumption can be partly reduced by complementing attitude thrusters with magnetic torquers (included in the simulated runs), and by exploiting the degrees of freedom offered by eight micro-thrusters versus the actuation of only five

force/torque components. A sub-optimal solution to this problem was mentioned in [4], but has not been implemented in the present case.
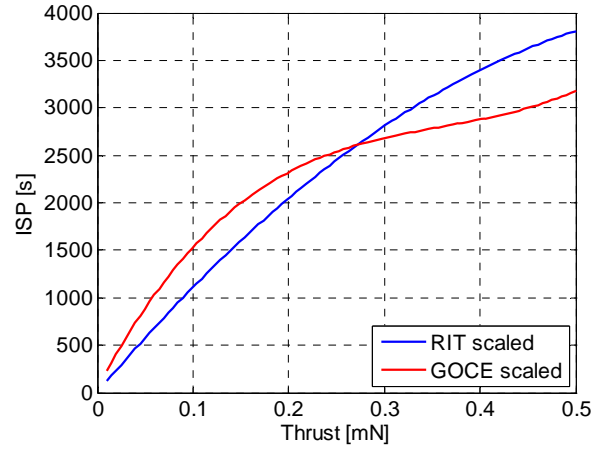

Figure 12 Micro-RIT and GOCE-type specific impulse profiles scaled to the same thrust

range.

Besides propellant saving, electric propulsion requires that average and peak electric power are minimized. The progressive 6-year average power to be supplied to the thruster assembly is shown in Figure 13. The total 6-year average must be read on the right asymptote: it stays below the target of 500 W. Instead, the peak power, not reported here, reached 1200 W, a rather demanding value.
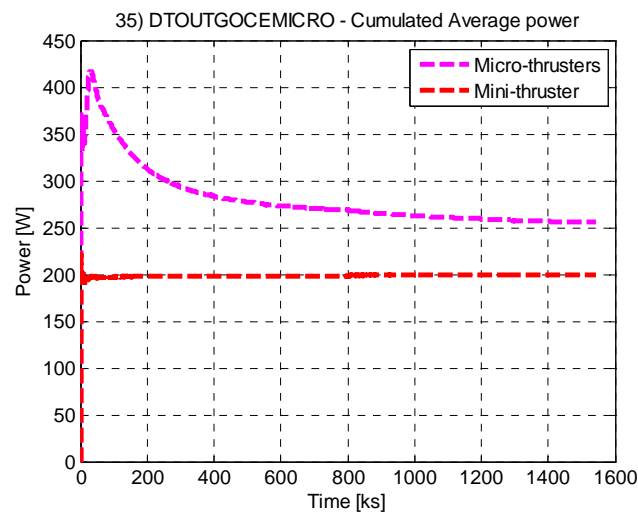

Figure 13 Progressive average electric power requested by mini and micro thrusters,

5   Conclusions

The paper outlines the formation control design and the simulated results, constrained by low command authority, formation box, drag-free bounds below $0.01\,\mu\text{m/s}^2$ in a mid frequency band around 1 mHz, and command decoupling from periodic input perturbations due to tide forces. Coupled with a low-Earth orbit and >10-km distance formation, the above requirements make the control design and the relevant technology challenging. The paper shows that formation fluctuations can be kept within the required box, also under worst-case environment conditions. They compete with formation control authority at the level of drag-free and attitude control, because of an all-propulsion mission. Further developments concern formation acquisition and fusion of the GPS metrology with the on-board optical metrology made available by satellite-to-satellite interferometry..

6   Acknowledgment

7   REFERENCES

[1] Cesare, S., Mottini, S., Musso, F., Parisch, M., Sechi G., Canuto, E., Aguirre, M., Leone, B., Massotti, L. and Silvestrin P., "Satellite formation for a next generation gravimetry mission", in R. Sandau et al. eds., Small satellite missions for Earth observations, Springer, Heidelberg, pp. 125-134, 2010.

[2] Tapley, B. D., Bettadpur, S., Watkins, M. and Reigber,C. "The gravity recovery and climate experiment: Mission overview and early results", Geophys. Res. Lett., Vol. 31, No. 9, May 2004.

[3] Fehringer, M., André, G., Lamarre, D. and Maeusli, D. "GOCE and its gravity measurement system", ESA Bulletin, Vol. 133, p. 15-23, February 2008.

[4] Canuto, E., "Drag-free and attitude control for the GOCE satellite", Automatica, Vol XLIV, No. 7, pp. 1766-1780, 2008.

[5] Loeb, H.W. "Development of RIT-microthrusters", Proc. 55th Int. Astronautical Congress 2004, 4-8 October 2004, Vancouver, Canada, paper IAC-04-S.4.04.

[6] Canuto, E. and Massotti, L., " All-propulsion design of the drag-free and attitude control of the European satellite GOCE", Acta Astronautica, Vol. LXIV, No. 2-3, pp. 325-344, 2009.

[7] Canuto, E., Molano-Jimenez, A. and Massotti, L., "Drag-free control of the GOCE satellite: noise and observer design", IEEE Trans. on Control System Technology, Vol. XVIII, No. 2, pp. 501-509, 2010.

[8] Kapila, V., Sparks, A.G., Buffington, J.M. and Yan Q., "Spacecraft formation flying: dynamics and control", J. Guidance, Control and Dynamics, Vol. XXIII, No. 2, pp. 561–564, 2000.

[9] Rossi, M. and Lovera, M., "A Predictive Approach to Formation Keeping for Constellations of Small Spacecrafts in Elliptical Orbits", in Proc. 5th International ESA Conference on GNC Systems, October 22-25, Frascati, Italy, 2002.

[10] Xu, Y., Fitz-Coy, N., Lind, R., and Tasch, A., "µ control for satellite formation flying", J. of Aerospace Engineering, Vol. XX, No. 1, pp. 10-21, 2007.

[11] Canuto, E., "Embedded Model Control: outline of the theory", ISA Transactions, Vol. XLIII, No. 3, pp. 363-377, 2007.

[12] Inalhan, G., Tillerson, M. and How, J.P., " Relative dynamics and control of spacecraft formations in eccentric orbits", J. Guidance, Control and Dynamics, Vol. XXV, No. 1, pp. 48-60, 2002.

[13] Schweighart S.A. and Sedwick R.J., "High-Fidelity Linearized J2 Model for Satellite Formation Flying", J. of Guidance, Control and Dynamics, Vol. XXV, No. 6, 2002.

[14] Canuto, E., Massotti, L., Molano-Jimenez, A. and Perez-Montenegro, C., "Drag-free and attitude control for long-distance, low-Earth-orbit, gravimetric satellite formation" in

Proc. 29th Chinese Control Conference (CCC 2010), Beijing, China, July 29-31, pp. 5408-5413, 2010.

[15] Canuto, E. and Massotti, L., "Local orbital frame predictor for LEO drag-free satellites" Acta Astronautica, Vol. LXVI, No. 3-4, pp. 446-454, 2010.

[16] Edwards, C.H., Wallace, N.C., Tato, C. and van Put, P. "The T5 ion propulsion assembly for drag compensation on GOCE", Proc. Second Int. GOCE user Workshop "GOCE. The geoid and oceanography", ESA-ESRIN, Frascati, Italy, 8-10 March 2004 (ESA SP-569, June 2004).

8   Appendix

Similar to [12] (equations (4) to (8)) and [13] (equations (9) to (13)), consider the k-th satellite moving in a perturbed orbit $\vec{r}_k$ with respect to a reference elliptic orbit of eccentricity $e \leq 0.005$ having radius

$$\vec{r} = r\vec{k}, \ \underline{r} = \underline{r}_0 / f(e,\theta), f(e,\theta) = (1+e\cos\theta)/(1-e^2) \tag{53}$$

and orbit rate and anomaly

$$\vec{\omega} = \dot{\theta}\vec{j}, \ \theta(t) = \theta_0 + \int_0^t \dot{\theta}(\tau)d\tau. \tag{54}$$

The perturbed coordinates are

$$\delta\vec{r}_k = \vec{r}_k - \underline{r} = \delta x_k \vec{i} + \delta y_k \vec{j} + \delta z_k \vec{k}. \tag{55}$$

The perturbation dynamics can be obtained through the following steps

1)   The total acceleration $\ddot{\vec{r}}_k$ is decomposed into reference and perturbed components, the latter being observed in the local orbiting frame

$$\ddot{\vec{r}}_k = \ddot{\underline{r}} + \delta\ddot{\vec{r}}_k + \vec{\omega}\times\delta\vec{r}_k + \vec{\underline{\omega}}\times(\vec{\underline{\omega}}\times\delta\vec{r}_k) + 2\vec{\underline{\omega}}\times\delta\dot{\vec{r}}_k \atop \ddot{\underline{r}} = \vec{\omega}\times(\vec{\omega}\times\underline{r}) \tag{56}$$

2)   The gravity acceleration $\vec{g}(\mathbf{r}_k)$ is decomposed into the spherical $\vec{g}(\mathbf{r}_k)$, J2 $\vec{g}_2(\mathbf{r}_k)$ and a higher order term $\delta\vec{g}(\mathbf{r}_k)$, and the former two components are expanded around the reference position $\underline{r}$ up to the 1st order term, thus obtaining

$$\vec{g}(\mathbf{r}) = \vec{g}_0(\mathbf{r}) + \vec{g}_2(\mathbf{r}) + \delta\vec{g}_2(\mathbf{r},\theta) + (U_0(\mathbf{r}) + U_2(\mathbf{r}))\delta\vec{r}_k + \delta\vec{g}(\mathbf{r}_k), \tag{57}$$

where U_0 and U_2 denote the gravity gradient tensor of the spherical and J2 components, and $\delta\vec{g}_2$ is the variable part of the J2 gravity acceleration. Introducing the Earth equatorial radius R_E, the orbit inclination i, the coefficient J_2, the mean orbit rate $\underline{\omega}_0$, and the coefficient ε_2, the constant term $\vec{g}_0 + \vec{g}_2$ having zero components except the radial is found to be written as

$$\begin{aligned}
\vec{g}_0 + \vec{g}_2 &= -\frac{\mu_E}{\underline{r}^3}\left(1 + \frac{3}{8}J_2\left(\frac{R_E}{\underline{r}}\right)^2(1+3\cos(2i))\right)r\vec{k} = \\
&= -\underline{\omega}_0^2(\underline{r}_0)f^3(e,\theta)\left(1 - \varepsilon_2(\underline{r}_0,R_E,J_2,i)f^2(e,\theta)\right)r\vec{k}
\end{aligned} \tag{58}$$

3) In the Newton equation $\ddot{\vec{r}}_k = \vec{g}(r_k) + \vec{a}_k$, where $\vec{a}_k$ accounts for non gravitational accelerations, the centrifugal and gravity accelerations are cancelled. Their equality defines the reference near-circular orbit in Figure 3 and the reference angular rate $\dot{\theta}$ as follows

$$\begin{aligned}
\dot{\theta}^2\vec{k} &= -\underline{\vec{\omega}}\times(\underline{\vec{\omega}}\times\vec{r})/\underline{r} = -\left(\vec{g}_0(\vec{r}) + g_2(\vec{r})\right)/\underline{r} = \\
&= \underline{\omega}_0^2 f^3(e,\theta)\left(1 - \varepsilon_2(i)f^2(e,\theta)\right)\vec{k}
\end{aligned}, \tag{59}$$

where the J2 coefficient $\varepsilon_2(i) < 10^{-3}$ applies to polar orbits with $i \cong \pi/2$.

4) Finally, $\dot{\theta}$ in (59) is expanded up to the first order of e and ε_2 providing

$$\dot{\theta} = \underline{\omega}_0\left(1 - \varepsilon_2/2 + 3e\cos\theta/2\right) + o\left(e^2,\varepsilon_2^2\right) = \underline{\omega} + 3e\underline{\omega}_0\cos\theta/2 + o\left(e^2,\varepsilon_2^2\right), \tag{60}$$

where $\underline{\omega}$ is the mean value of $\dot{\theta}$.

Dropping the equality (59) in (56), the perturbed dynamics with respect to the reference near-circular orbit of radius $\underline{\vec{r}}$ (point $\underline{C}$ in Figure 3) reads as

$$\begin{aligned}
\delta\ddot{\vec{r}}_k &= -\ddot{\theta}\underline{j}\times\delta\vec{r}_k - \underline{\vec{\omega}}\times(\underline{\vec{\omega}}\times\delta\vec{r}_k) - 2\underline{\vec{\omega}}\times\delta\dot{\vec{r}}_k + \\
&+ \delta\vec{g}_2(\mathbf{r},\theta) + (U_0(\mathbf{r}) + U_2(\mathbf{r},\theta))\delta\vec{r}_k + \delta\vec{g}(\mathbf{r}_k) + \vec{a}_k
\end{aligned}. \tag{61}$$

Formation dynamics keeps the same form as (61) upon replacement of the differential vectors in (61) with

$$\Delta \vec{r} = \delta \vec{r}_0 - \delta \vec{r}_1 = \Delta x \vec{i} + \Delta y \vec{j} + \Delta z \vec{k}$$
$$\Delta \vec{a} = \vec{a}_0 - \vec{a}_1, \ \Delta \vec{g} = \delta \vec{g}(\mathbf{r}_0) - \delta \vec{g}(\mathbf{r}_1)$$

(62)

and upon the cancellation of the J2 periodic component $\delta \vec{g}_2$. Figure 3 shows that

$$\Delta \vec{r}_k = \delta \vec{r}_k + \delta \vec{r},$$

(63)

where $\delta \vec{r}$ is the formation CoM perturbation. Thus the formation differential position can be referred to the formation CoM C instead of the reference point $\underline{C}$, which implies the alternative definition

$$\Delta \vec{r} = \Delta \vec{r}_0 - \Delta \vec{r}_1.$$

(64)

The reference point $\underline{C}$ favours linearization, whereas formation CoM C is measurable from GPS.

The gravity tensors in (61)can be written as

$$U_0(\underline{r}) = -\omega_0^2 f^3(e, \theta) D_0$$
$$U_2(\underline{r}, \theta) = \omega_0^2 f^3(e, \theta) \varepsilon_2 \left(D_2 + f^2(e, \theta) \Delta U_2(\theta) \right)$$

(65)

where assuming the coordinate order of (2), D_0, D_2 are diagonal constant matrices, and ΔU_2 is aperiodic matrix that can be found to be [13]

$$D_0 = \begin{bmatrix} 1 & 0 & 0 \\ 0 & -2 & 0 \\ 0 & 0 & 1 \end{bmatrix}, \ D_2 = \begin{bmatrix} 1 & 0 & 0 \\ 0 & -4 & 0 \\ 0 & 0 & 3 \end{bmatrix}$$

$$\Delta U_2(\theta) \cong \begin{bmatrix} -7\cos 2\theta & 8\sin 2\theta & 0 \\ 8\sin 2\theta & 12\cos 2\theta & 0 \\ 0 & 0 & -5\cos 2\theta \end{bmatrix}, \ @i \cong \pi/2$$

(66)

Defining the rate vectors

$$\Delta v_x = \Delta \dot{x} + 2\dot{\theta}\Delta z, \ \Delta v_y = \Delta \dot{y}, \ \Delta v_z = \Delta \dot{z},$$

(67)

and separating longitudinal/radial and cross-track dynamics, the formation state equations read as

$$
\begin{bmatrix} \Delta \dot{x} \\ \Delta \dot{v}_x \\ \Delta \dot{z} \\ \Delta \dot{v}_z \end{bmatrix} = \begin{bmatrix} 0 & 1 & \vdots & -2\dot{\theta} & 0 \\ -g_{xx}(\theta) & 0 & \vdots & \ddot{\theta}+g_{xz}(\theta) & 0 \\ \cdots & \cdots & \vdots & \cdots & \cdots \\ 0 & 0 & \vdots & 0 & 1 \\ \ddot{\theta}+g_{zx}(\theta) & 2\dot{\theta} & \vdots & -\dot{\theta}_z^2 & 0 \end{bmatrix} \begin{bmatrix} \Delta x \\ \Delta v_x \\ \Delta z \\ \Delta v_z \end{bmatrix} + \begin{bmatrix} 0 \\ \Delta a_x \\ 0 \\ \Delta a_z \end{bmatrix},
$$

$$
\begin{bmatrix} \Delta \dot{y} \\ \Delta \dot{v}_y \end{bmatrix} = \begin{bmatrix} 0 & 1 \\ -\dot{\theta}_y^2 & 0 \end{bmatrix} \begin{bmatrix} \Delta y \\ \Delta v_y \end{bmatrix} + \begin{bmatrix} 0 \\ \Delta a_y \end{bmatrix}
$$

(68)

where $\Delta a_j = \Delta u_j + d_j$, $j = x, y, z$ is the sum of the formation command Δu_j and a generic disturbance d_j. The periodic terms in (66) have been either collected in g_{xx}, g_{xz} and g_{zx}, or hidden in the squared angular frequencies $\dot{\theta}_y^2$ and $\dot{\theta}_z^2$.

The state matrices in (68) are periodic in the anomaly θ. The same form as in (68) is kept if longitudinal and radial coordinates are converted to LORF coordinates by means of the reference flight-path angle $\underline{\gamma}$ defined by

$$
\sin \underline{\gamma} = \dot{\underline{r}} / |\dot{\underline{r}}|, \ \dot{\underline{\gamma}} = e\underline{\omega}_0 \cos\theta \left(1 + o(e)\right).
$$

(69)

Hence $\dot{\theta}$ in (60) slightly modifies together with all the functions of θ in (68), but the mean value $\underline{\omega}$ remains the same. Since the zero-mean periodic coefficients in (68) can be developed in series as

$$
\begin{aligned}
g(\theta) &= \underline{\omega}_0^2 e \sum_{k=1}^{\infty} \gamma_{ek} \sin(k\theta + \varphi_k) + \\
&+ \underline{\omega}_0^2 \varepsilon_2 \sum_{k=1}^{\infty} \gamma_{\varepsilon k} \sin(k\theta + \psi_k), \ e|\gamma_{ek}|, \varepsilon_2 |\gamma_{\varepsilon k}| < \varepsilon = 0.01
\end{aligned}
$$

(70)

and their magnitude is bounded by

$$
|g(\theta)| \le \varepsilon \underline{\omega}_0^2, \ \varepsilon \le 0.01,
$$

(71)

they can be dropped from the state matrices in view of the control design, and treated as periodic input perturbations to be rejected by formation control. The design model in (6) is obtained by replacing $\dot{\theta}_z$, $\dot{\theta}_y$ and $\dot{\theta}$ in (68) with their mean values

$$
\underline{\omega} = \underline{\omega}_O \sqrt{1 - \varepsilon_2}, \ \underline{\omega}_z = \underline{\omega}_O \sqrt{1 + \varepsilon_2}, \ \underline{\omega}_y = \underline{\omega}_O \sqrt{1 - 3\varepsilon_2},
$$

(72)

and by collecting the periodic terms in the forcing vector

$$\mathbf{g}(\theta) = \begin{bmatrix} -g_{xx}\Delta x + \left(\ddot{\theta} + g_{xz}\right)\Delta z + ... \\ \left(\ddot{\theta} + g_{zx}\right)\Delta x - \left(\dot{\theta}_z^2 - \underline{\omega}_z^2\right)\Delta z + ... \\ -\left(\dot{\theta}_y^2 - \underline{\omega}_y^2\right)\Delta z + ... \end{bmatrix} \cong d \begin{bmatrix} -g_{xx} \\ \ddot{\theta} + g_{zx} \\ 0 \end{bmatrix}, \tag{73}$$

where the approximation in the right-hand side is allowed by $|\Delta x| \cong d \gg |\Delta y|, |\Delta z|$, and the suspension points account for higher order gravity anomalies.